**Helmholtz-Zentrum Dresden-Rossendorf (HZDR)**

# Nanometer-scale characterization of laser-driven compression, shocks, and phase transitions, by x-ray scattering using free electron lasers

Perma-Link to Publication Repository of HZDR:

https://www.hzdr.de/publications/Publ-26231

# Nanometer-scale characterization of laser-driven compression, shocks and phase transitions, by X-ray scattering using free electron lasers

T. Kluge,[1,a)] C. Rödel,[2,3] M. Rödel,[1,4] A. Pelka,[1] E. E. McBride,[3,b)] L. B. Fletcher,[3,c)] M. Harmand,[5] A. Krygier,[5] A. Higginbotham,[6] M. Bussmann,[1] E. Galtier,[3] E. Gamboa,[3] A. L. Garcia,[1] M. Garten,[1,4] S. H. Glenzer,[3] E. Granados,[3] C. Gutt,[7] H. J. Lee,[3] B. Nagler,[3] W. Schumaker,[8] F. Tavella,[3] M. Zacharias,[1,4] U. Schramm[1,4] and T. E. Cowan[1,4]

[1]Helmholtz-Zentrum Dresden – Rossendorf, Bautzner Landstraße 400, 01328 Dresden, Germany
[2]University of Jena, Max-Wien-Platz 1, 07743 Jena, Germany
[3]SLAC National Accelerator Laboratory, Menlo Park, CA 94025, USA
[4]Technische Universität Dresden, 01069 Dresden, Germany
[5]Universite Pierre et Marie Curei, 75005 Paris, France
[6]University of York, YO10 5DD York, United Kingdom
[7]Universität Siegen, 57068 Siegen, Germany
[8]Stanford University, Stanford, CA 94305, USA

We study the feasibility of using small angle X-ray scattering (SAXS) as a new experimental diagnostic for intense laser-solid interactions. By using X-ray pulses from a hard X-ray free electron laser we can simultaneously achieve nanometer and femtosecond resolution of laser-driven samples. This is an important new capability for the Helmholtz International Beamline for Extreme Fields (HIBEF) at the HED endstation currently built at the European XFEL. We review the relevant SAXS theory and its application to transient processes in solid density plasmas and report on first experimental results that confirm the feasibility of the method. We present results of two test experiments where the first experiment employs ultra-short laser pulses for studying relativistic laser plasma interactions, and the second one focuses on shock compression studies with a nanosecond laser system.

---

[a)] Author to whom correspondence should be addressed. Electronic mail: t.kluge@hzdr.de.

[b)] Principal investigator of the nanosecond laser beam time LH88 at MEC/LCLS (SLAC), E. McBride was with DESY, Hamburg, Germany at that time.

[c)] Principal investigator of the ultra-short laser beam time LF20 at MEC/LCLS (SLAC).

# I. INTRODUCTION

This work discusses the development of small angle X-ray scattering (SAXS) as a new tool to characterize and follow the evolution of nanoscale features in solid-density plasma and in matter under extreme conditions driven by high intensity and high power lasers. Laser-plasma SAXS will be one component in helping to realize what we hope will become a revolution in experimental High Energy Density (HED) science through the coupling of ultra-high-intensity and high-energy lasers with brilliant X-ray Free Electron Laser (XFEL) light sources. This will become an important part of the new HIBEF (Helmholtz International Beamline for Extreme Fields) [1] at the HED Instrument of the European XFEL, and will build upon the work presented in the following which was begun at the MEC endstation[2] of the Linear Coherent Light Source (LCLS)[3].

Research in laser-driven HED science is developing rapidly and is making contributions in a variety of areas ranging from plasma astrophysics[4] and fusion energy[5], to compact particle acceleration[6]–[9], short wavelength radiation generation[10], materials dynamics[11] and the exploration of new phases of matter[12]. Laser-driven HED plasmas and materials driven to high pressures are very complicated physical systems, characterized by a wide range of simultaneously occurring fundamental processes, many of which involve states far from equilibrium. It is in general very difficult to isolate the individual contributing processes experimentally, and the theoretical verification of our understanding of HED physics requires extensive simulations, often spanning wide spatial and temporal scales. One important motivation for HED science at XFELs is therefore to make use of many high precision X-ray techniques, which are not possible at laser-only facilities, to identify and track the evolution of specific processes embedded within the complex environment of high-power laser-driven matter.

In this work we are specifically targeting processes on the sub-micron to nanometer spatial scale, which is set by the typical bulk response of plasma at solid density (10-100 nm). Some of the many examples include hot electron generation [13]–[15] and transport [16], [17], plasma ionization and opacity [18], ablation [19], [20], hole-boring [21]–[23], instabilities [24]–[32], high harmonic generation (HHG) at surfaces [10], shocks [33]–[35], pressure induced phase changes, precipitation of crystallites of new high-pressure phases following shock[36], high-strain-rate materials damage, and the Equation of State of matter under compression[37].

These types of phenomena are actively studied at high power laser-only facilities, using a variety of optical, x-ray and particle diagnostic techniques, including both self-emission and active probing methods. These include X-ray absorption spectroscopy and phase contrast imaging (PCI)[37], [38], X-ray Thomson scattering[39]–[41], X-ray diffraction or wide angle X-ray scattering (WAXS) [42], [43], self-emission X-ray spectroscopy and x-ray imaging[44], optical probing[45], proton radiography [46], transient imaging[47] and deflectometry[48] and less direct probes such as harmonic generation [49], [50], and particle acceleration or nuclear reactions[51].

Synchronized laser-driven X-ray back-lighters are particularly important as penetrating probes of the atomic and plasma conditions inside of the HED-driven sample. They typically require substantial laser energy to produce a sufficiently bright source, and complex target assemblies for the backlighter foils and shine shields. Most importantly, the X-ray spatial resolution is generally limited to >10 µm, and the temporal resolution to several ps, due to the electron transport and relaxation dynamics in the backlighter target. By comparison laser-drvien HED experiments at X-ray FEL's offer the advantage of improved time structure (down to few fs), precise positioning (sub µm), extreme brightness for single-shot and photon-hungry techniques, and almost full coherence for advanced diffraction and holographic techniques. For example, sub-micron spatial resolution down to circa 500 nm has already been demonstrated for a laser-driven shock wave by Phase Contrast Imaging[37]. .

Tens of nanometer resolution has also been impressively demonstrated in laser ablation by Coherent X-ray diffraction imaging (CXDI) in the soft x-ray range in experiments at FLASH[52]–[54]. Diffraction encodes the electron density correlations in the sample into the angular distribution of scattering intensity on a 2D imaging detector via the momentum transfer $\vec{q}$ between X-ray photons and electrons Figure 1. CXDI allows a full real-space image reconstruction of the sample by iterative phase retrieval, and such techniques are being aggressively pursued toward the development of single molecule imaging, including substantial work on "diffract and destroy" and important effects associated with the ionization of the target molecule by the XFEL beam[55].

For many of the fundamental processes that are of interest in laser-driven HED physics, a full real space reconstruction is not required. Often it is more convenient to work in reciprocal space and analyze the scattering intensity as a function of $\vec{q}$ to identify the characteristic spatial frequencies $\kappa$ of a given feature or instability. Its growth rate $\Gamma(\kappa, t)$ and

temporal evolution can be measured directly by the scattering intensity at a given $\vec{q}$ at different times after the drive laser by pump probe techniques. A great deal of information then can already be extracted directly from the X-ray scattering data, when characteristic features can be identified in reciprocal space with predictive plasma simulation and modeling. As shown in Refs [56], [57] these can include processes such as plasma ablation and laser hole-boring, surface instabilities, electron transport instabilities, filamentation, and ionization dynamics, all of which occur on the spatial scale of micron to few nm in relativistic laser-matter interactions. Nanometer scale phenomena are also important also in non-relativistic laser experiments such as shock compression and high pressure phase transitions. For example, the intrinsic width of a shock front may relate to the viscosity in the equation of states (EOS) of warm dense matter (WDM)[37], and the formation and evolution of a new phase from a nucleation site in compressed matter can be viewed as the appearance and growth of nanoscale crystallites[36].

In these cases, small angle X-ray scattering (SAXS) is sufficient to provide the $\vec{q}$-space intensity information necessary to identify and follow the evolution of specific plasma features, without the need for oversampling and full phase reconstruction. This significantly simplifies the experimental requirements as compared to CXDI, and is quite well matched to the demands and challenges of high-power laser experiments.

Moreover, SAXS – in contrast to phase contrast imaging (PCI) or direct radiography – exhibits negligible blur at the cost of losing the absolute positioning information. This is true since SAXS is sensitive to time-integrated correlations of spatial features rather than the time-integrated spatial features. Assuming a fast moving feature with temporally constant shape (e.g. surface plasmons), PCI or radiography would blur the image to the temporal average the time needed to traverse the feature plus the X-ray pulse duration. For SAXS the blurring would be given only over the much shorter time it takes the X-ray beam to traverse the feature, since the correlations of the feature (and hence the SAXS signal) remain constant throughout the probe duration. This enables completely new structural diagnostic insights in dynamic systems, for example the production of higher harmonics (HHG) through analysis of surface plasmons during intense optical laser incidence.

In this paper we expand upon the initial concepts presented in Refs [56], [57], and demonstrate the feasibility of performing SAXS on high-power laser-driven samples to extract nm-scale information, in two experiments performed at LCLS. In the following sections, we survey some of the laser-plasma processes of specific interest, we review the relevant scattering theory in plasmas, we elucidate some specific observables found in the X-ray scattering distribution, and we present the application of SAXS to two examples, namely short pulse laser ablation and long-pulse laser compression.

## II. THEORETICAL BACKGROUND
## A. Plasma dynamics under laser irradiation
### 1. Ultra-short ultra-intense lasers

The interaction of ultra-high intensity (UHI) lasers with solids exhibits complex and nonlinear electron and ion dynamics. Most prominently, the laser can ionize the front surface and accelerate electrons from a foil that in turn can leave the front surface and move ballistically through the bulk. For small laser electric field strength $E_0$ and linear polarization, i.e. laser strength parameter $a_0 = E_0 e / m_e \omega_0 c \ll 1$, the laser field strength decays inside the plasma as an evanescent wave and the electrons oscillate in the direction of the electric field vector. When the laser is incident obliquely to the solid, electrons are pulled in the vacuum direction once every laser period and are then pushed back and leave the laser interaction region when the laser electric field changes its sign. This process is called Brunel acceleration[58]. Other electron acceleration mechanisms include resonance absorption[59] and, for relativistic laser intensities ($a_0 \gg 1$), $\vec{j} \times \vec{B}$ acceleration[60] and direct laser acceleration[8], [61]. Other important effects are the hole boring process, where the longitudinal component of the laser Lorentz force pushes the target front surface and accelerates it inside the target, ablation, and electro-static shock generation and propagation.

Several nonlinear effects and instabilities can develop in the relativistic case, generating a complex and seemingly chaotic parameter space. Plasmons, parametric instabilities[13], [29], [62] and Rayleigh-Taylor-like (RT) instabilities[30], [31] seeded for example by a parametric instability[32] can break up an otherwise flat target front surface and cause density ripples, with growth times on the order of few to tens of femtoseconds only. Nonlinear relativistic electron motion can give rise to HHG and preplasma development by heating and expansion of the front skin layer. This can considerably enhance or decrease laser absorption into energetic electrons accelerated into the plasma [63] generating large current densities exceeding $10^{13} \text{A/cm}^2$ which can excite plasma oscillations [64] and generate resistive magnetic fields [16], [65] inside the bulk. If strong enough, they may not be perfectly balanced anymore by the bulk return current resulting for example in
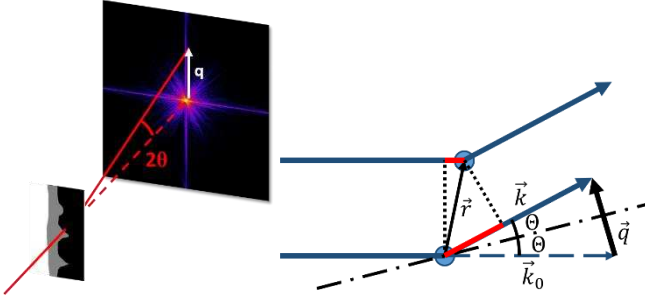
Figure 1: Scattering geometry for SAXS. XFEL is incident from left.

beam filamentation of relativistic laser-generated electrons inside the solid or behind [24]–[27].

All those effects have in common that they occur quickly (on the time scale of the optical laser, or plasma period) and on small scales (plasma wavelength of a few 10s to a few hundred nanometers), which can be uniquely explored by SAXS using XFEL pulses. Such fast processes in the intermediate regime between micron and angstrom scale are not well explored experimentally with existing techniques. Likewise, a direct experimental comparison to simulations and analytic models could help to strengthen and push their predictive capability.

## 2. High-energy long-pulse lasers

SAXS can also be a valuable tool for the class of nanosecond laser compression and shock experiments studying for example the phase diagram of materials or other pressure release mechanisms after compression. Those mechanisms as well as a precise knowledge of the EOS of the key constituents are of fundamental interest for many areas of physics, e.g. planetary laboratory astrophysics [4] or material physics [11], and in our specific experiment presented later in this paper for an example for the study of a technologically important material like Si. For example, the phase transition sequence that Si undergoes under static compression conditions on compression and decompression is well established, yet numerous shock compression studies show disagreement concerning the onset of the semi-conductor to metallic transition [66].

To-date, these studies have focused on the low decompression rates accessible using diamond anvil cell techniques, with no in-situ studies performed at high strain-rates i.e. under release from laser-driven shock compression. Optical nanosecond, high energy laser pulses can drive shock waves into solid materials to high pressures of few 10 GPa. The non-hydrodynamic conditions can induce dynamic strain and rapid strain release. The dynamics of such a compression wave – with subsequent elastic, plastic and phase transition

responses to release strain [12] – was imaged with phase contrast imaging only recently [37]. With its much higher spatial resolution SAXS could help to analyze structures such as grain sizes, interfaces between composites, edge sharpness of phase transition grain boundaries, fractures or the shock front, or plastic/elastic responses to shock induced or phonon induced strain and release. The results can give information about the EOS: For example, as mentioned before, the intrinsic width of a shock front may relate to the viscosity in the EOS, and pump-probe measuring the phonons could be used to calculate the ion sound velocity and hence temperature (transition from phonons to ion acoustic waves), with high spatial resolution, as a complementary method to X-ray Thomson scattering, emission measurements [67] or Bragg scattering [68].

## B. Small angle X-ray scattering in laser plasmas

Neglecting electron-electron and electron-ion correlations, the scattering cross section of all electrons can be described by the Thomson formula $d\sigma/d\Omega = r_e^2(1 + \cos^2 2\theta)/2$, which for small scattering angles $\theta$ is simply the square of the classical electron radius $r_e = e^2/4\pi\varepsilon_0 m_e c^2$. However, especially at X-ray energies around electronic transition energies, electron-ion correlations cannot be neglected since electrons cannot vibrate freely in the laser field as they experience the nuclear field. In that case the scattering cross section needs certain corrections to account for photoionization and photoexcitation at bound-bound resonances as will be discussed later.

For pure Thomson scattering, the amplitude of the scattered wave $f = \varphi \exp(i\varphi)$ at small angle reads

$$\varphi = \varphi_i \left(\frac{d\sigma}{d^2 d\Omega}\right)^{1/2} \cong \varphi_i \frac{r_e}{d} \qquad (1)$$

where $\varphi_i$ is the amplitude of the incoming X-ray wave which we for now assume to be fully coherent (plane wave), and $d$ is the distance of the detector to the scattering electron.

The diffraction signal on a detector is given by the interference of scattered waves. The phase difference of two scattered waves originating from two electrons separated by $\vec{r}$ and reaching the detector at the same position is seen from a simple geometric construction to be $\varphi = -\vec{r}(\vec{k} - \vec{k}_0) \equiv -\vec{r}\vec{q}$ if $d$ is large compared to $|\vec{r}|$ (see Figure 1)[69]. Here, $\vec{k}_0 = \vec{e}_z E_0/\hbar c$ is the wave vector of the incident X-ray beam with photon energy $E_0$, and $\vec{k} = \vec{e}_{2\theta} E/\hbar c$ is the wave vector of the scattered beam with scattered photon energy $E$. The momentum transfer $\vec{q}$ is named as scattering vector with $|\vec{q}| = 2\vec{k} \sin\theta$. Since in the limit of $\theta \ll 1$ the energy transfer to the scattering electron is negligible, the scattering is elastic,

$E'_\gamma = E_\gamma$ and $|\vec{k}_0| = |\vec{k}|$. Assuming each photon is scattered only once, the total interference pattern is given by the integral over all scattered waves originating in the scattering object (neglecting a constant offset in time for the light propagation from the sample to the detector),

$$\phi(\vec{q}, t) = \frac{r_e}{d} \int \phi_i(\vec{r}, \tau(z)) n(\vec{r}, \tau(z)) e^{-i\vec{q}\vec{r}} \, d^3r \qquad (2)$$

where $n(\vec{r}, \tau(z))$ is the density of scatterers at position $\vec{r}$ relative to an arbitrary origin at time $\tau(z) = t + \frac{z}{c}$, and is considered to vary only slowly with time. With that we mean that the density (and $\phi_i$) be constant on time scales of the X-ray period. The intensity $I = \phi^2$ measured on the detector is finally given by the absolute square of the amplitude.

To take ionization and bound-bound resonances into account it is now helpful to split the electron density into a free electron component $n_{e,free}$ of electrons that can move freely inside the sample and electrons bound to atoms or ions, $n_{e,bound}$. For the sake of simplicity we assume that only one ion species is present, the electron distribution inside an ion is spherically symmetric and $\phi_i$ is spatially constant. The integral in Eqn. (2) can then be split into a part over the ion density $n_{ion}$, which is the ion structure factor $S_{ion}(\vec{q}) = \int n_{ion}(\vec{r}, t) \exp(-i\vec{q}\vec{r}) \, d^3r$, and a part over electrons within an ion, which is the ion form factor $F_{ion}$. Taking advantage of the scattering vector length being small and hence typically much smaller than the reciprocal ion size, the ion form factor neglecting bound-bound and bound-free resonances,

$$F_{ion}(\vec{q}) = \int_{ion} n_e(\vec{r}) \exp(-i\vec{q}\vec{r}) \, d^3r, \qquad (3)$$

is given simply by the number of bound electrons $F_{ion,\Gamma}(\vec{q}) \cong \Gamma \equiv Z - Q$. The instantaneous scattered intensity then reads

$$I(\vec{q}) = \left(\frac{r_e\phi}{d}\right)^2 \left(S_{free}(\vec{q}) \, F_{free} + S_{ion}(\vec{q}) \, F_{ion}\right)^2. \qquad (4)$$

Generally, more than one ion species is present and $\phi_0$ is not spatially constant. Then, the density of scattering centers $n$ in Eqn. (2) can simply be replaced by

$$n = n_{e,free} + \sum_\Gamma n_{ion,\Gamma}\Gamma + \sum_\gamma n_{ion,\gamma} F_{ion,\gamma}^{res}(E_0). \qquad (5)$$

Here we add the ion form factor optical correction (i.e. the resonant contribution) to the non-resonant part describing the Thomson scattering on bound electrons. The complex valued, X-ray energy dependent resonant contribution $F_{ion,\gamma}^{res} = F'_{ion,\gamma} + iF''_{ion,\gamma}$ arises due to absorption at bound-bound resonances and bound-free transitions and for a given element depends mainly on the number $\gamma$ of electrons in the shells relevant for nuclear potential screening during a transition. Since in contrast to Thomson scattering no $\pi/2$ phase shift between the incoming and scattered wave exists, the opacity is proportional to the imaginary part of the optical correction, $\tau(E_0) = 4\pi c r_e \hbar d E_0^{-1} \sum_\gamma n_{ion,\gamma} F''_{ion,\gamma}$[70] which for thermal equilibrium can be calculated with specialized codes, e.g. SCFLY[71]. The real part of the optical correction then follows from the Kramer-Kronig relation.

The less electrons there are in the screening shells, the higher is the transition energy, providing for the ion species specificity when tuning the X-ray energy to a specific energy. This fact is employed in resonant SAXS, also called resonant coherent X-ray diffraction (RCXD). By tuning the X-ray energy to a specific bound-bound resonance, a specific inner electron occupancy number can be selected. The optical correction to the ion form factor can then be orders of magnitude larger than the single electron form factor, then dominating the scattering signal and allowing to measure the spatial distribution of the specific ion species.

Since we consider only small scattering angles $2\theta \ll 1$, the scattering vector length in beam direction $z$ can often be neglected, $zq_z = 0$, simplifying the integral in Eqn. (2) in $z$-direction to a simple projection of the electron density weighted by the X-ray wave amplitude along the X-ray beam axis. However, it is important to note that this is not possible for thick targets where the phase difference of waves scattered at different depths can become non-negligible, i.e. $2z \sin^2 \theta \sim O(\lambda)$. In the following we limit ourselves to $q_z = 0$, $\vec{q} \equiv (q_x, q_y)$. Then, (5) is equal to the well-known relation for the number $N = I \cdot d^2 \Delta\Omega$ of photons scattered into $\Delta\Omega$,

$$N(\vec{q}, t) = \frac{N_{i,0}}{A_i} \left(\frac{d\sigma}{d\Omega}\right) \left|FT\left(\sqrt{g} \, \tilde{n}\right)\right|^2 \Delta\Omega \qquad (6)$$

where $N_{i,0}$ and $A_i$ are the incoming number of photons and illuminated area, $g(x,y)$ is a normalized function with $= \int_{A_i} g(x,y) \, dxdy = 1$, describing the spatial distribution of incoming photons, $\tilde{n}$ is the areal scatter center density taking into account the time retardation, and $\Delta\Omega = \Delta\varphi\Delta\theta \cong \Delta q_y \Delta q_z / k^2 \cos(\theta)$ is constant to first order of $\theta$.

In contrast to the majority of systems studied with SAXS such as molecules in solution or samples in statistical motion, for the case of laser generated plasmas or shocked solids we cannot assume a statistically isotropic system in space or time. Therefore, the Fourier integral in Eqn. (2) cannot be reduced to an integral over the distance only. Typically in any non-crystalline sample there exists no long range order. In such a case the contribution of the background to the scattering signal can be neglected and only density

5

differences are significant (except for very small angles not relevant for the experiment).

The X-ray source can be treated as a non-invading probe beam as long as the areal density of incoming X-ray photons is small enough to only affect a minority of ions (in the case of RCXD), and to not heat the sample to a point that it affects the expansion during the probe time. The first condition can be written as $N_{i,0}/A_i \ll (\sigma_{bf} + \sigma_{bb})^{-1} = n_{ion}/(r_e^2 \sum_\gamma n_{ion,\gamma} F_{ion,\gamma}^{res})$. As an example we consider an X-ray spot size of order 10 μm and photon energy 8 keV, as used in the experiments presented in Sec. III. A relevant material for RCXD at that energy would for example be Copper, $\sigma_{bf} \approx 4 \cdot 10^3$ barn. Then, the number of photons per pulse is limited to $N_{i,0} \ll 10^{15}$.

The latter condition, which is the relevant condition for our experiments, means that we require the additional expansion $\Delta s \approx (c_s(T + T_X) - c_s(T))\tau_X$ due to the additional temperature $T_X$ introduced to the plasma by photo-ionization to be below the precision of the measurement ($c_s(T) \cong (Zk_BT/M)$ is the ion sound velocity, $T$ is the plasma electron temperature and $M$ is the ion mass). Then we can derive a condition for the maximum allowed number of photons. Again assuming an X-ray energy of just below the cold Cu K$\alpha$ edge, 8 keV, the energy for a photo-electron from the L shell is roughly $E_P = E_x - E_L \approx 7 \, keV$ and $T_X = E_P N_{i,0} \sigma_{Lf}/A_i Q$, where the average ionization degree of the Cu ions is $Q \approx 10 \dots 20$ for typical few 100 eV plasma temperatures. If we require $\Delta s$ to be less than a nanometer, then for an XFEL spot size of order 10 μm and 40 fs duration one requires $N_{i,0} < 10^{14}$. Since $c_s(T)$, $\sigma_{Lf}$ and $Q$, as an order of magnitude estimate, are largely independent of the ion species within a large range, the heating and hence plasma expansion are also, and the above estimate can be seen as a general limit.

Current XFEL sources and those under construction deliver up to $10^{12}$ photons per pulse, fulfilling both requirements. Only when using micron or few nanometer X-ray foci the interaction of the X-ray with the probe needs to be considered. For the experiments presented in Sec. III, even though the XFEL introduces significant additional heat and ionization, we can ignore the effects on the measurement.

For reference, before proceeding we give the scattering intensity from Eqn. (4) in scaled quantities, and specifically for a pixel detector (pixel size $A_D = a_D^2$). We first note that $\vec{q}$ can simply be transformed to detector spatial coordinates $\vec{R} = \vec{q}d/k$, hence a detector pixel corresponds to
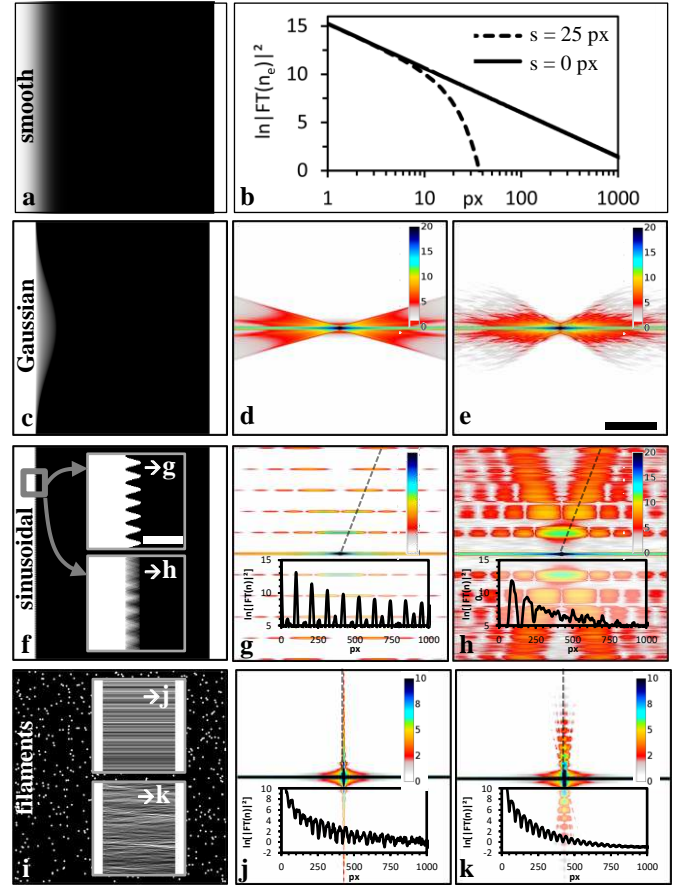


Figure 2: Left row: Typical UHI laser generated plasma distributions projected along the XFEL direction assuming UHI incident from left (a, c, f) or view along UHI axis (i). Middle and right row: Respective PS. (a) Smooth surface (Eq. 10). (b) PS for s = 0 (solid), s = 25 px (dashed). (c) Gaussian dent. (d) PS assuming the dent is perfectly flat and (e) having a sinusoidal check board pattern, e.g. due to a RT instability. (f) Flat surface with sinusoidal ripples extending through the whole projection depth (top inset) or only 1/10, repeating through the full depth with random phase and frequency (bottom inset). (g, h) show respective PS. (i) Filaments extending through the foil normal to the foil surface (top inset) or with a FWHM deflection of 5° (bottom inset). (j, k) Respective PS. Insets: Vertical profiles along dashed lines. All densities normalized to 1px⁻¹, black bar is 250 px, white bar 50 px. Details see main text. With Eqn. (7) we can give absolute photon numbers, e.g. assuming $N_i = 10^{11}$, full ionization with $n_e = 0.7 \cdot 10^{25} cm^{-3}$, plasma size of $\Delta x = \Delta y = \Delta z = (2048 \, px)^3 = (5 \, \mu m)^3$, $E_0 = 8 \, keV$, detector with pixel size $a_D = 10 \, \mu m$ situated $d = 1 \, m$ behind the scattering target. Then, $\tilde{n}_e[px^{-1}] = n_e[\mu m^{-3}] a_{FFT}^2 \Delta z[\mu m] = 10^5$ and $G = 3.3 \cdot 10^{-18}$, hence a PS value of $\exp(10)$ at pixel $s_{PS} = 100$ would correspond to $N = N_i G \exp(13) \tilde{n}_e[px^{-1}] \approx 750$ photons in the detector pixel located $s_D = \Delta q_{PS}/\Delta q_D = 309$ pixels from the XFEL beam axis.

$\Delta q_D = a_D k/d$. We now take $\sqrt{g} \, \tilde{n}[cm^{-2}]$ on an $S \times S$ matrix with $S \equiv \sqrt{A_i[\mu m^2]} /a_{PS}$ where $a_{PS} = \mu m/px$ is the matrix pixel size in units of micron. When the Fourier

transform is performed numerically the result is again an $S \times S$ matrix with a pixel size $\Delta q_{PS} = 2\pi/\sqrt{A_i}$. The number $N(\vec{R})$ of photons scattered into detector pixel $\vec{s}_D = (s_x, s_y)$ located at position $\vec{R} = (R_x, R_y) = \vec{s}_D a_D$ relative to the point where the XFEL intersects the detector plane then is proportional to the numerical FT absolute square, taken at pixel $\vec{s}_{PS} = \vec{s}_D \Delta q_D / \Delta q_{PS} = 807 \cdot 10^{-6} E_0[keV] \vec{s}_D \sqrt{A_i[\mu m^2]} a_D[\mu m]/ d[m]$. The factor of proportionality is

$$G = \frac{N_{i,0}}{A_i} \left( \frac{r_e a_D a_{PS}}{d} \right)^2 = \left( 2.82 \cdot 10^{-7} \frac{a_D[\mu m]}{S \, d[m]} \right)^2. \quad (7)$$

SAXS and the resonant variant RCXD promise a wide range of plasma properties to become accessible with nanometer and femtosecond resolution. This includes the mode structure of the opacity, ion distribution and – with phase reconstruction techniques reconstructing the real and imaginary part of the optical corrections independently – also the plasma electron energy distribution[57] since the ratio $F''_{ion}/F'_{ion}$ depends on the energy distribution. RCXD offers the prospect of direct in situ experimental tests of ionization models and ion dynamics in kinetic plasma codes, or analytic approximations. In combination with SAXS it could therefore offer the long sought direct link between simulations of ultra-short ultra-intense laser solid interaction and subsequent relativistic electron transport and interaction with and ionization of the solid, which would be necessary to reach the goal of reliable predictive simulations in the future.

### Examples for typical scattering patterns

In order to illustrate the wide range of possibilities SAXS and similar scattering techniques may offer in laser-plasma experiment diagnostics, we produced a few exemplary SAXS patterns from various characteristic synthetic cases, see Figure 2. A more comprehensive and general collection of geometries and respective SAXS patterns can be found in [72, Ch. 16]. The Figure comprises the generic cases of (a) a flat surface with smooth surface, (c) a surface with Gaussian dent as it can be produced e.g. by UHI hole boring,(f) a surface with a sinusoidal modulation e.g. generated by a RT instability (modulation amplitude 50 nm and spatial frequency 0.02 nm$^{-1}$) and (i) filaments extending through the foil (filament diameter 50 nm, average nearest neighbor distance 100 nm). Many other, more complex patterns generated by UHI laser-solid interaction or laser-driven

shocks can be derived from those cases, or are a combination or variation, for example buried gratings expanding due to collisional heating are a convolution of (a) and (f).

It can be seen that the characteristic well-known scattering patterns can be clearly distinguished, even in the not-so-perfect cases of a mix of spatial frequencies and amplitudes of the sinusoidal surface modulations, or non-parallel and intersecting filaments inside the foil (average angle 5°). Moreover, by fitting with the theoretical patterns one can extract the characteristic properties and derive the underlying physical quantities characterizing the electron distributions, such as the range of spatial frequencies and amplitudes of surface modulations (from the spacing, orientation and vertical/ horizontal width of scattering maxima; see panels g, h), distance, divergence and size of filament channels (vertical spacing, opening angle and intensity profile of scattering maxima; panels j, k) or the expansion scale s of a smooth surface and hole boring depth D, even without a full numerical phase retrieval.

We will demonstrate this in the following in detail on the last two examples: smoothness and hole boring depth of a surface. We start with the connection between $I(q)$ and interface sharpness $s$ considering a single planar density interface in the projection along the X-ray direction. Such a step gives rise to a streak in the SAXS pattern in perpendicular direction. The length and width of such streak correspond to sharpness of the density gradient and size of the plane. For a 1D density step in x-direction of infinite sharpness it is $I(q_x) \propto |FT[\Theta(x)]|^2 = 2/\pi q_x^2$.[1] The intensity for any density step being smoother falls faster with $q_x$, e.g. for an error function with width $s$ the intensity falls proportional to

$$\left| FT\left[ erf(x/\sqrt{2}s) \right] \right|^2 = \frac{2}{\pi q_x^2} e^{-q_x^2 s^2}. \quad (8)$$

This relation explains the drop of the intensity of the smooth surface compared to the step-like one, Figure 2 b).

Important physical examples of density interfaces can be found in the class of energetic nanosecond laser pulses interacting with a solid target. Compressed material, but also material that has undergone a strain releasing phase transition, or fractures, as well as surface deformations, material interfaces and different compression wave velocities due to different sound speeds in composite materials all

---

[1] Note, that this differs from Porod's law $I \propto q^{-4}$ due to our definition of the detector being in the y-z-plane and a single spatially fixed step. For Porod's law one assumes a solution

of many identical objects and the detector to be in the x-y plane (with x‖surface, which in our case is the step, see [74] p. 92f) and averages over all possible orientations of the surface (Eqn. 3.3 in [75]).

constitute density gradients. Such density distribution could be for example the compression front itself, fractures[73] or phase transition bands[36]. A similar expression as Eqn. (8) can be derived also for rough surfaces of varying height $h(y,z)$, replacing the width $s$ with the mean surface height $s \rightarrow \sqrt{\langle h^2 \rangle}$. Since graded surfaces in this respect give the same qualitative scattering pattern as rough surfaces, we use the two synonymous in the following.

In many cases one might consider 3D rotationally symmetric surfaces, such as a cone shaped surface. Then the scattered photon intensities decrease more quickly along the streaks perpendicular to the projection of the surface of revolution for both the step-like and error function density profiles than in the 1D case, $I(q_\perp) \propto 1/q_\perp^3$ and $I(q_\perp) \propto \exp(-q_\perp^2 s^2)/q_\perp^3$, respectively. Generally and more realistically the surface will neither be 1D nor perfectly rotationally symmetric, hence the power of q in the denominator is between 2 and 3. However, an upper limit for the sharpness $s$ can always be given from a fit with the 1D equation (8)) as all cases show a quicker intensity drop with $q_\perp$ for given $s$ and hence would yield a smaller fit value for $s$.

Panels c-e of Figure 2 show an exemplary SAXS $\vec{q}$-space pattern that can be expected for the probably most abundant structure in ultra-intense laser-solid interaction, the laser hole boring dent a the target front surface. Assuming the area of 2048 px x 2048 px corresponds to 5 μm x 5 μm ($a_{FFT} = 0$), the Gaussian dent shown in panel a would have a 1σ width of 1 μm and depth of 500 nm. As can be seen in the power spectrum panel (b), the dent generates a continuum of scattered photons bounded in $\vec{q}$-space by diagonals through the origin at an angle α. The angle of the diagonals corresponds to the angle of the tangent of inflection to the dent. Hence, if for example the width $\sigma$ of the dent was known, the hole boring velocity could be calculated from its depth D, assuming a Gaussian profile,

$$D = e^{1/2} \sigma \tan \alpha. \qquad (9)$$

It should be noted, that the photon distribution within the bounding diagonals will mostly occur not as continuous but rather as set of distinct lines since the surface will not be perfectly smooth as in the example but will have some inhomogeneities. This is illustrated in panel (c) where we assumed a sinusoidal check board pattern modulating the otherwise smooth dent with an amplitude of 1/10 of the local depth of the dent and a spatial frequency of 0.002 px$^{-1}$ (2 μm$^{-1}$ in the above example). Again, the dashed lines mark the angle of the tangent of infliction, this time to Gaussian dent with the sinusoidal hump on top.
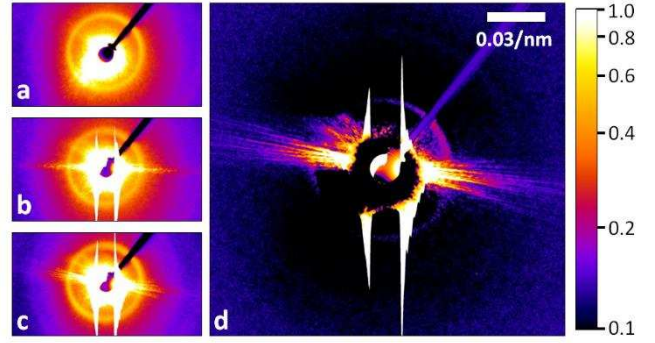


Figure 3: Normalized SAXS patterns recorded from (a) an XFEL-only without wire target, and (b) 10 mJ and (c), (d) 200 mJ optical laser irradiation of a 5 μm wire target. (d) shows the same shot as (c) with the background from the XFEL-only shot subtracted. The ring in the background originates from scattering of the XFEL beam in the Kapton exit window of the vacuum chamber.

With the SAXS method it is feasible to detect a wide range of plasmonic and filamentation processes and allow for the characterization of their spatial distribution and – with pump-probe – also of their temporal evolution and growth rate, even without a full numerical phase retrieval. Nanometer resolution can be expected when sufficiently large q-values are observed.

For small feature sizes of few Angstrom and below the scattering angles of few keV X-rays become too large for the linearization assumed for SAXS to hold and the scattering transitions to WAXS, while on the other side for micron scale features the scattering angle becomes ultra-small and PCI would be a preferred imaging method.

## III. EXPERIMENTAL DEMONSTRATION

To demonstrate the experimental feasibility of SAXS at laser-driven solids and solid plasmas, we set up a small angle scattering detector at LCLS MEC end station. In two separate beam times we acquired data from an ultra-short pulse drive laser and a nanosecond drive laser.

### A. Ultra-short ultra-intense lasers

In the first beam time, an aluminum wire target was irradiated by a Ti:Sa laser pulse with a duration of 60 fs, energy of 200 mJ before compression which was focused on a spot of 3 μm × 5 μm, resulting in an intensity of $1.3 \cdot 10^{19}$ W/cm$^2$. The laser pulse was circularly polarized, resulting in a dimensionless laser strength parameter $a_0 = 1.7$. The target wire radius was 5 μm. The XFEL beam probe was aligned 45° with respect to the UHI laser axis in the plane perpendicular to the wire axis. The X-ray energy was 5.5 keV corresponding to a wavelength $\lambda = 0.23$ nm, the pulse
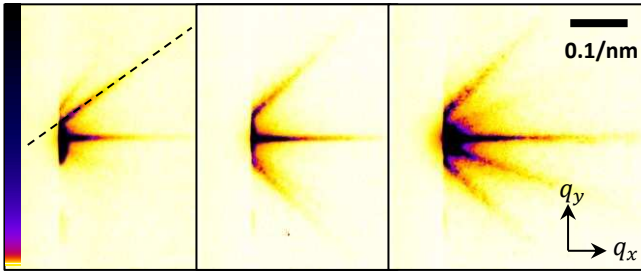
Figure 4: Examplary SAXS pattern recorded during shock compression with the XFEL being aligned normal to the drive laser. Similar patterns for similar nominal laser and target parameters were consistently observed in all our shots with reproducible angles of the streaks. Left part was covered by an absorber to avoid oversaturation. The dashed line marks the position of the cut analyzed exemplary in Figure 5.

duration was 62 fs and arrival time on target was 72 ps after the UHI laser pulse. The XFEL pulse energy was 3.37 mJ, which equals $3.8 \cdot 10^{12}$ photons per pulse. It was focused by a beryllium lens to approximately 5 µm to 10 µm, the target was positioned in the focal plane. In order to constrain the X-ray irradiation area on target to a limited field of view, an aperture with square opening was positioned between the lens and the target. Its sides were rotated by 45° with respect to the wire axis to have the scattering of residual X-ray intensity hitting the aperture walls be oriented 45° with respect to the wire axis and not interfering with the scattering from the wire itself at 90°.

Figure 3 shows the scattering pattern recorded by a PIXIS-XF camera with 13.5 µm pixel size, positioned 4.15 m down the X-ray direction outside the vacuum. The X-ray pulse was transported up to a few cm in front of the detector about 4m through vacuum, exiting in air through a Kapton window. The direct beam was blocked outside the vacuum by a steel ball beamstop of diameter 2.5 mm. Figure 3a shows the background scattering consisting of diffuse slit scattering of the apertures positioned under 45° and scattering in the Kapton vacuum chamber window. Panel (b) shows the scattering pattern of the un-driven wire with negligible UHI laser irradiation (20 mJ pulse energy). Strong scattering in the horizontal direction can be seen that we attribute to scattering of the XFEL beam on the aluminum wire positioned vertically. In panel c) the scattering pattern recorded at full UHI intensity is shown, to our knowledge the first published SAXS pattern of a solid plasma driven by a UHI laser, and panel d) shows the same shot where the background from (a) was subtracted.

The patterns clearly show a transition from wire scattering along the horizontal axis in the un-driven case to a bow-tie like pattern of several individual streaks. We notice the striking similarity to the expected pattern from a dent, shown in Figure 2c. We can use Eqn. (9) and calculate the dent
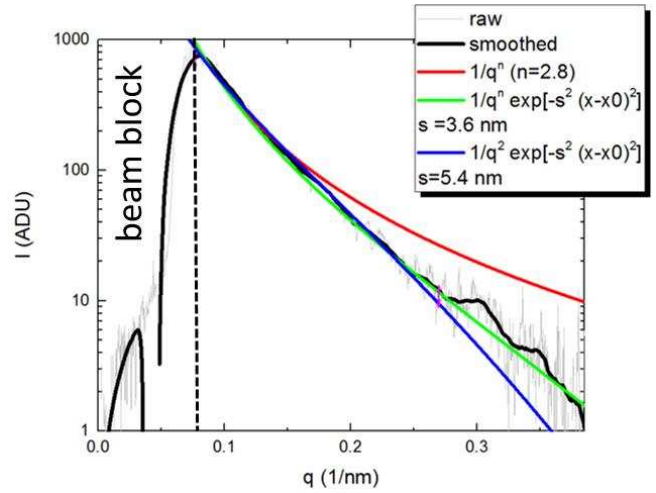


Figure 5: Cut through the streak of Figure 4 along the dashed line (gray) and fits with a 1D model assuming a step-like density interface (red), a smooth interface following an error function (blue) and a smooth interface with rotational symmetry (green).

depth. From the bow-tie half opening angle of approximately $\beta = 9°$ it follows that the depth would be approximately 0.9 µm which for the 72 ps delay between UHI laser irradiation and X-ray arrival translates into an average surface velocity of $3.8 \cdot 10^{-5}$c. It is worth noting that since the laser intensity was barely relativistic, this surface recession is possibly not dominated by laser hole-boring but rather might be due to thermal expansion and ablation effects. However, there is no model or simulation method available to make quantitative predictions for the two at the long delay after the main pulse interaction that would allow for a clear discrimination.

## B. High-energy long-pulse lasers

The second demonstration of the feasibility of SAXS measurements we present here was in an experiment focused on crystallographic structure changes of silicon, shock compressed by an optical laser with pulse length 20 ns, diameter 250 µm, $\lambda = 527$ nm and energy 1 J to 20 J. The setup chosen for this experiment stands out due to its transverse geometry of the optical laser and XFEL. The weakly focused XFEL projects through the target perpendicular to the optical laser axis and shock wave propagation direction, so that uncompressed, compressed and release volumes can be distinguished. The X-ray photon energy was set to 9.5 keV with diameter between 5 µm and 10 µm, and pulse length 39 fs. The direct beam was blocked inside the vacuum before the Kapton window with a knife edge. The target was 300 $\mu m$ thick and consisted of 125 $\mu m$ polycrystalline silicon, tampered by two layers of single crystalline silicon of 125 $\mu m$ each.
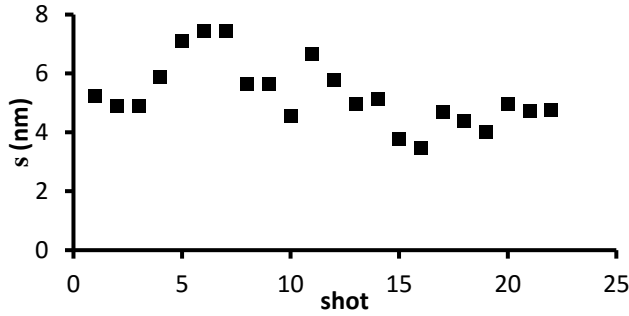
Figure 6: Maximum density scale length σ, obtained by fitting the streaks with Eqn. (8) (1D model). The laser and target parameters were similar for all shots.

The optical laser impinges on the sandwiched target side head on in the central polycrystalline area. It initiates a shock, propagating parallel to the tamper layers and normal to the X-ray direction. The XFEL pulse probes a small region of $10 \, \mu m$ diameter at 60 µm down into the target. The delay with respect to the drive laser was set to match the shock wave arrival time at the X-ray position and was scanned between 12 ns to 24 ns. By classical X-ray diffraction it is possible to distinguish between the crystallographic phases. The original simple cubic diamond (cd) phase is indicated by Bragg peaks that originate from the large grains in the polycrystalline layer. As the strain and release was studied in this experiment, the delay was varied to obtain the series of release waves. Upon compression, a transition can be observed from distinct Bragg peaks to rings. Those results and details about the shock parameters will be subject of a forthcoming paper. As described in Sec. IIB, we can expect to see streaks in the SAXS signal, originating from density steps induced by the shock compression or release through a number of processes. To discriminate between them, more evidence and diagnostics is needed. Here we report on the SAXS measurements only in the context of the technical feasibility.

In Figure 4 we show three representative SAXS patterns with a single streak, two symmetric streaks or even more streaks. The angles under which those streaks occur are constant throughout all shots; the integrated signal intensity is correlated with the integrated WAXS signal in the high pressure rings, confirming the XFEL timing to shock arrival. From this correlation between the SAXS streak and high-pressure WAXS ring we infer that the SAXS streaks may be due to scattering either from the high pressure region, i.e. from phase transitions, fractures or the shock front itself, or from other correlated mechanisms.

We analyzed the profile along a streak in the SAXS pattern in order to obtain information about the microscopic density profile of the scattering source. Figure 5 shows the profile of the streak shown in the left panel of Figure 4. The

low photon background enables us to count individual photons, enabling us to use a wide q-range for fitting with sample profiles. The blue line is a fit with the scattering intensity profile expected for a planar 1 dimensional error-function-like density jump. The fitted width $s$ of the density interface is 5.4 nm, but the fit underestimates the intensity seen at large q-values. The red line is the fit assuming a step-like density profile, i.e. $q^{-n}$ with free exponent to allow for a variable geometry between 1D ($n = 2$) and rotationally symmetric ($n = 3$). The best fit is obtained for $n = 2.8$ which is in good agreement with a density profile rotationally symmetric around the laser axis. However, the disagreement with the measurement at large scattering vector length is significant and demonstrates that the profile is not step-like. Finally, we did a fit for the intensity expected for an erf-shaped density profile, this time allowing the exponent n of q to vary (green line). The fitted density width now is $s = 3.6$ nm and the fit agrees almost perfectly with the measurement throughout the full q range. The same analysis was done for all shots showing streaks in the SAXS data. We find a very reproducible upper limit for the density length scale $s$ in the range between 3 nm and 8 nm, Fig. 6. The fluctuations are not given by the SAXS uncertainty but rather are inherent to the physical processes or initial conditions e.g. of the drive laser or target.

## IV. CONCLUSIONS AND OUTLOOK

X-ray scattering techniques will without doubt drive our understanding in many areas of ultra-intense, ultra-short or high energy laser-solid interaction. The short duration of XFEL pulses, together with its penetrating power through solids and solid plasmas and large transverse coherence, enable the direct probing of many properties of the laser matter interaction and material or plasma response. XRTS, WAXS and PCI are all well-established techniques and we have shown the potential of SAXS in filling the gap for scales relevant for many processes in ultra-intense laser-solid physics but also in compressed materials.

First pilot experiments have already shown that the relevant q-range is accessible and can be applied to the width of density gradients in shocked materials or laser-generated dents in solids, e.g. generated by ablation or hole-boring. We observed a low, single-photon background that enabled us to determine the sharpness of density steps observed during the ns-laser compression of Si targets to less than 10 nm, not being limited by the detector resolution.

Resonant scattering off partially ionized plasmas and opacity measurements with both high spatial and temporal resolution make the SAXS technique a platform for

10

validating not only solid state and plasma physical models, but allows also to test microscopic and atomic physics models & codes under highly non-thermal, non-equilibrium, femtosecond transient high-field, high-current situations.

## REFERENCES

[1] HIBEF Consortium, "http://www.hibef.eu." .

[2] S. H. Glenzer, "Matter under extreme conditions experiments at the Linac Coherent Light Source."

[3] P. Emma, R. Akre, J. Arthur, R. Bionta, C. Bostedt, J. Bozek, A. Brachmann, P. Bucksbaum, R. Coffee, F.-J. Decker, Y. Ding, D. Dowell, S. Edstrom, A. Fisher, J. Frisch, S. Gilevich, J. Hastings, G. Hays, P. Hering, Z. Huang, R. Iverson, H. Loos, M. Messerschmidt, A. Miahnahri, S. Moeller, H.-D. Nuhn, G. Pile, D. Ratner, J. Rzepiela, D. Schultz, T. Smith, P. Stefan, H. Tompkins, J. Turner, J. Welch, W. White, J. Wu, G. Yocky, and J. Galayda, "First lasing and operation of an ångstrom-wavelength free-electron laser," Nat. Photonics, vol. 4, no. 9, pp. 641–647, Aug. 2010.

[4] A. Benuzzi-Mounaix, S. Mazevet, A. Ravasio, T. Vinci, A. Denoeud, M. Koenig, N. Amadou, E. Brambrink, F. Festa, A. Levy, M. Harmand, S. Brygoo, G. Huser, V. Recoules, J. Bouchet, G. Morard, F. Guyot, T. de Resseguier, K. Myanishi, N. Ozaki, F. Dorchies, J. Gaudin, P.

M. Leguay, O. Peyrusse, O. Henry, D. Raffestin, S. Le Pape, R. Smith, and R. Musella, "Progress in warm dense matter study with applications to planetology," Phys. Scr., vol. T161, p. 14060, 2014.

[5] M. Tabak, P. A. Norreys, V. T. Tikhonchuk, and K. A. Tanaka, "Alternative ignition schemes in inertial confinement fusion," Nucl. Fusion, vol. 54, no. 5, p. 54001, 2014.

[6] R. A. Snavely, M. H. Key, S. P. Hatchett, I. E. Cowan, M. Roth, T. W. Phillips, M. A. Stoyer, E. A. Henry, T. C. Sangster, M. S. Singh, S. C. Wilks, A. MacKinnon, A. Offenberger, D. M. Pennington, K. Yasuike, A. B. Langdon, B. F. Lasinski, J. Johnson, M. D. Perry, and E. M. Campbell, "Intense high-energy proton beams from petawatt-laser irradiation of solids," Phys. Rev. Lett., vol. 85, no. 14, pp. 2945–2948, 2000.

[7] A. Maksimchuk, S. Gu, K. Flippo, D. Umstadter, and V. Bychenkov, "Forward ion acceleration in thin films driven by a high-intensity laser," Phys. Rev. Lett., vol. 84, no. 18, pp. 4108–11, May 2000.

[8] S. A. Gaillard, T. Kluge, K. A. Flippo, M. Bussmann, B. Gall, T. Lockard, M. Geissel, D. T. Offermann, M. Schollmeier, Y. Sentoku, and T. E. Cowan, "Increased laser-accelerated proton energies via direct laser-light-pressure acceleration of electrons in microcone targets," Phys. Plasmas, vol. 18, no. 5, p. 56710, 2011.

[9] F. Wagner, O. Deppert, C. Brabetz, P. Fiala, A. Kleinschmidt, P. Poth, V. A. Schanz, A. Tebartz, B. Zielbauer, M. Roth, T. St??hlker, and V. Bagnoud, "Maximum Proton Energy above 85 MeV from the Relativistic Interaction of Laser Pulses with Micrometer Thick CH2 Targets," Phys. Rev. Lett., vol. 116, no. 20, p. 205002, 2016.

[10] U. Teubner and P. Gibbon, "High-order harmonics from laser-irradiated plasma surfaces," Rev. Mod. Phys., vol. 81, no. 2, pp. 445–479, Apr. 2009.

[11] D. Kraus, J. Vorberger, J. Helfrich, D. O. Gericke, B. Bachmann, V. Bagnoud, B. Barbrel, A. BlaŽêvić, D. C. Carroll, W. Cayzac, T. Döppner, L. B. Fletcher, A. Frank, S. Frydrych, E. J. Gamboa, M. Gauthier, S. Göde, E. Granados, G. Gregori, N. J. Hartley, B. Kettle, H. J. Lee, B. Nagler, P. Neumayer, M. M. Notley, A. Ortner, A. Otten, A. Ravasio, D. Riley, F. Roth, G. Schaumann, D. Schumacher, W. Schumaker, K. Siegenthaler, C. Spindloe, F. Wagner, K. Wünsch, S. H. Glenzer, M. Roth,

and R. W. Falcone, "The complex ion structure of warm dense carbon measured by spectrally resolved x-ray scattering," Phys. Plasmas, vol. 22, no. 5, 2015.

[12] W. H. Gust and E. B. Royce, "Axial yield strengths and two successive phase transition stresses for crystalline silicon," J. Appl. Phys., vol. 42, no. 5, pp. 1897–1905, 1971.

[13] T. Kluge, T. Cowan, A. Debus, U. Schramm, K. Zeil, and M. Bussmann, "Electron temperature scaling in laser interaction with solids," Phys. Rev. Lett., vol. 107, no. 20, p. 205003, Nov. 2011.

[14] A. Debayle, J. Sanz, L. Gremillet, and K. Mima, "Toward a self-consistent model of the interaction between an ultra-intense, normally incident laser pulse with an overdense plasma," Phys. Plasmas, vol. 20, no. 5, p. 53107, 2013.

[15] T. Kluge, M. Bussmann, T. E. Cowan, and U. Schramm, "Controlled electron bunch generation in the few-cycle ultra-intense laser???solid interaction scenario," Nucl. Instruments Methods Phys. Res. Sect. A Accel. Spectrometers, Detect. Assoc. Equip., vol. 829, pp. 376–377, 2016.

[16] P. Leblanc and Y. Sentoku, "Scaling of resistive guiding of laser-driven fast-electron currents in solid targets," Phys. Rev. E - Stat. Nonlinear, Soft Matter Phys., vol. 89, no. 2, p. 23109, Feb. 2014.

[17] H. Nishimura, R. Mishra, S. Ohshima, H. Nakamura, M. Tanabe, T. Fujiwara, N. Yamamoto, S. Fujioka, D. Batani, M. Veltcheva, T. Desai, R. Jafer, T. Kawamura, Y. Sentoku, R. Mancini, P. Hakel, F. Koike, and K. Mima, "Energy transport and isochoric heating of a low-Z, reduced-mass target irradiated with a high intensity laser pulse," Phys. Plasmas, vol. 18, no. 2, p. 22702, Feb. 2011.

[18] M. Garten, "Comparing field ionization models in simulations of laser-matter interaction," TU Dresden, 2013.

[19] P. Mora, "Thin-foil expansion into a vacuum," AIP Conf. Proc., vol. 827, no. 18, pp. 227–236, May 2006.

[20] P. Mora, "Thin-foil expansion into a vacuum," AIP Conf. Proc., vol. 827, no. 5, pp. 227–236, 2006.

[21] M. Tabak, J. Hammer, M. E. Glinsky, W. L. Kruer, S. C. Wilks, J. Woodworth, E. M. Campbell, M. D. Perry, and R. J. Mason, "Ignition and high gain with ultrapowerful

lasers*," Phys. Plasmas, vol. 1, no. 5, pp. 1626–1634, 1994.

[22] A. Pukhov and J. Meyer-ter-Vehn, "Laser Hole Boring into Overdense Plasma and Relativistic Electron Currents for Fast Ignition of ICF Targets," Phys. Rev. Lett., vol. 79, no. 14, pp. 2686–2689, 1997.

[23] A. P. L. Robinson, "Production of high energy protons with hole-boring radiation pressure acceleration," Phys. Plasmas, vol. 18, no. 5, pp. 18–23, 2011.

[24] A. Bret, M. C. Firpo, and C. Deutsch, "Collective electromagnetic modes for beam-plasma interaction in the whole k space," Phys. Rev. E - Stat. Nonlinear, Soft Matter Phys., vol. 70, no. 4 2, pp. 1–15, 2004.

[25] M. S. Wei, F. N. Beg, E. L. Clark, A. E. Dangor, R. G. Evans, A. Gopal, K. W. D. Ledingham, P. McKenna, P. A. Norreys, M. Tatarakis, M. Zepf, and K. Krushelnick, "Observations of the filamentation of high-intensity laser-produced electron beams," Phys. Rev. E - Stat. Nonlinear, Soft Matter Phys., vol. 70, no. 5 2, p. 56412, 2004.

[26] A. Bret, M. C. Firpo, and C. Deutsch, "Characterization of the initial filamentation of a relativistic electron beam passing through a plasma," Phys. Rev. Lett., vol. 94, no. 11, pp. 1–4, 2005.

[27] J. Metzkes, T. Kluge, K. Zeil, M. Bussmann, S. D. Kraft, T. E. Cowan, and U. Schramm, "Experimental observation of transverse modulations in laser-driven proton beams," New J. Phys., vol. 16, no. 2, p. 23008, Feb. 2014.

[28] Y. Sentoku, K. Mima, S. Kojima, and H. Ruhl, "Magnetic instability by the relativistic laser pulses in overdense plasmas," Phys. Plasmas, vol. 7, no. 2, pp. 689–695, 2000.

[29] A. Macchi, F. Cornolti, F. Pegoraro, T. V. Liseikina, H. Ruhl, and V. A. Vshivkov, "Surface Oscillations in Overdense Plasmas Irradiated by Ultrashort Laser Pulses," Phys. Rev. Lett., vol. 87, no. 20, p. 205004, Oct. 2001.

[30] C. A. J. Palmer, J. Schreiber, S. R. Nagel, N. P. Dover, C. Bellei, F. N. Beg, S. Bott, R. J. Clarke, A. E. Dangor, S. M. Hassan, P. Hilz, D. Jung, S. Kneip, S. P. D. Mangles, K. L. Lancaster, A. Rehman, A. P. L. Robinson, C. Spindloe, J. Szerypo, M. Tatarakis, M. Yeung, M. Zepf, and Z. Najmudin, "Rayleigh-Taylor instability of an ultrathin foil accelerated by the radiation pressure of an intense laser," Phys.

Rev. Lett., vol. 108, no. 22, p. 225002, May 2012.

[31] A. Sgattoni, S. Sinigardi, L. Fedeli, F. Pegoraro, and A. Macchi, "Laser-driven Rayleigh-Taylor instability: Plasmonic effects and three-dimensional structures," Phys. Rev. E - Stat. Nonlinear, Soft Matter Phys., vol. 91, no. 1, pp. 1–6, 2015.

[32] T. Kluge, J. Metzkes, K. Zeil, M. Bussmann, U. Schramm, and T. E. Cowan, "Two surface plasmon decay of plasma oscillations," Phys. Plasmas, vol. 22, no. 6, p. 64502, 2015.

[33] J. Denavit, "Absorption of high-intensity subpicosecond lasers on solid density targets," Phys. Rev. Lett., vol. 69, no. 21, pp. 3052–3055, 1992.

[34] L. O. Silva, M. Marti, J. R. Davies, R. A. Fonseca, C. Ren, F. S. Tsung, and W. B. Mori, "Proton Shock Acceleration in Laser-Plasma Interactions," Phys. Rev. Lett., vol. 92, no. 1, p. 15002, Jan. 2004.

[35] M. S. Wei, S. P. D. Mangles, Z. Najmudin, B. Wallon, A. Gopal, M. Tatarakis, A. E. Dangor, E. L. Clark, R. G. Evans, S. Fritzler, R. J. Clarke, C. Hernandez-Gomez, D. Neely, W. Mori, M. Tzoufras, and K. Krushelnick, "Ion acceleration by collisionless shocks in high-intensity-laser- underdense-plasma interaction," Phys. Rev. Lett., vol. 93, no. 15, p. 155003, 2004.

[36] G. Mogni, A. Higginbotham, K. Gaál-Nagy, N. Park, and J. S. Wark, "Molecular dynamics simulations of shock-compressed single-crystal silicon," Phys. Rev. B, vol. 89, no. 6, p. 64104, 2014.

[37] A. Schropp, R. Hoppe, V. Meier, J. Patommel, F. Seiboth, Y. Ping, D. G. Hicks, M. A. Beckwith, G. W. Collins, A. Higginbotham, J. S. Wark, H. J. Lee, B. Nagler, E. C. Galtier, B. Arnold, U. Zastrau, J. B. Hastings, and C. G. Schroer, "Imaging Shock Waves in Diamond with Both High Temporal and Spatial Resolution at an XFEL," Sci. Rep., vol. 5, p. 11089, 2015.

[38] S. Kneip, C. McGuffey, F. Dollar, M. S. Bloom, V. Chvykov, G. Kalintchenko, K. Krushelnick, A. Maksimchuk, S. P. D. Mangles, T. Matsuoka, Z. Najmudin, C. A. J. Palmer, J. Schreiber, W. Schumaker, A. G. R. Thomas, and V. Yanovsky, "X-ray phase contrast imaging of biological specimens with femtosecond pulses of betatron radiation from a compact laser plasma wakefield accelerator,"

Appl. Phys. Lett., vol. 99, no. 9, p. 93701, 2011.

[39] G. Gregori, S. H. Glenzer, F. J. Rogers, S. M. Pollaine, O. L. Landen, C. Blancard, G. Faussurier, P. Renaudin, S. Kuhlbrodt, and R. Redmer, "Electronic structure measurements of dense plasmas," Phys. Plasmas, vol. 11, no. 5 PART 2, pp. 2754–2762, 2004.

[40] R. Redmer, H. Reinholz, G. Röpke, R. Thiele, and A. Höll, "Theory of X-ray Thomson scattering in dense plasmas," IEEE Trans. Plasma Sci., vol. 33, no. 1 I, pp. 77–84, 2005.

[41] S. H. Glenzer and R. Redmer, "X-ray Thomson scattering in high energy density plasmas," Rev. Mod. Phys., vol. 81, no. 4, pp. 1625–1663, Dec. 2009.

[42] M. Gauthier, L. B. Fletcher, A. Ravasio, E. Galtier, E. J. Gamboa, E. Granados, J. B. Hastings, P. Heimann, H. J. Lee, B. Nagler, A. Schropp, A. Gleason, T. Döppner, S. Lepape, T. Ma, A. Pak, M. J. Macdonald, S. Ali, B. Barbrel, R. Falcone, D. Kraus, Z. Chen, M. Mo, M. Wei, and S. H. Glenzer, "New experimental platform to study high density laser-compressed matter," Rev. Sci. Instrum., vol. 85, no. 11, p. 11E616, Nov. 2014.

[43] L. B. Fletcher, H. J. Lee, T. Döppner, E. Galtier, B. Nagler, P. Heimann, C. Fortmann, S. LePape, T. Ma, M. Millot, A. Pak, D. Turnbull, D. A. Chapman, D. O. Gericke, J. Vorberger, T. White, G. Gregori, M. Wei, B. Barbrel, R. W. Falcone, C.-C. Kao, H. Nuhn, J. Welch, U. Zastrau, P. Neumayer, J. B. Hastings, and S. H. Glenzer, "Ultrabright X-ray laser scattering for dynamic warm dense matter physics," Nat. Photonics, vol. 9, no. 4, pp. 274–279, 2015.

[44] E. Stambulchik, E. Kroupp, Y. Maron, U. Zastrau, I. Uschmann, and G. G. Paulus, "Absorption-aided x-ray emission tomography of planar targets," Phys. Plasmas, vol. 21, no. 3, 2014.

[45] J. Metzkes, K. Zeil, S. D. Kraft, M. Rehwald, T. E. Cowan, and U. Schramm, "Reflective optical probing of laser-driven plasmas at the rear surface of solid targets," Plasma Phys. Control. Fusion, vol. 58, no. 3, p. 34012, 2016.

[46] R. Jafer, L. Volpe, D. Batani, M. Koenig, S. Baton, E. Brambrink, F. Perez, F. Dorchies, J. J. Santos, C. Fourment, S. Hulin, P. Nicolai, B. Vauzour, K. Lancaster, M. Galimberti, R. Heathcote, M. Tolley, C. Spindloe, P. Koester, L. Labate, L. Gizzi, C. Benedetti, A. Sgattoni, M. Richetta, J. Pasley, F. Beg, S. Chawla, D. Higginson, A. MacKinnon, A. McPhee, D. H.

13

Kwon, and Y. Ree, "Proton radiography of a laser-driven cylindrical implosion," AIP Conf. Proc., vol. 1209, no. 4, pp. 47–50, Jul. 2010.

[47]  M. Borghesi, A. Schiavi, D. H. Campbell, M. G. Haines, O. Willi, A. J. MacKinnon, P. Patel, M. Galimberti, and L. A. Gizzi, "Proton imaging detection of transient electromagnetic fields in laser-plasma interactions (invited)," Rev. Sci. Instrum., vol. 74, no. 3 II, pp. 1688–1693, 2003.

[48]  A. J. Mackinnon, P. K. Patel, R. P. Town, M. J. Edwards, T. Phillips, S. C. Lerner, D. W. Price, D. Hicks, M. H. Key, S. Hatchett, S. C. Wilks, M. Borghesi, L. Romagnani, S. Kar, T. Toncian, G. Pretzler, O. Willi, M. Koenig, E. Martinolli, S. Lepape, A. Benuzzi-Mounaix, P. Audebert, J. C. Gauthier, J. King, R. Snavely, R. R. Freeman, and T. Boehlly, "Proton radiography as an electromagnetic field and density perturbation diagnostic (invited)," Rev. Sci. Instrum., vol. 75, no. 10 II, pp. 3531–3536, 2004.

[49]  D. An Der Br??gge, N. Kumar, A. Pukhov, and C. R??del, "Influence of surface waves on plasma high-order harmonic generation," Phys. Rev. Lett., vol. 108, no. 12, p. 125002, Mar. 2012.

[50]  C. R??del, D. An Der Br??gge, J. Bierbach, M. Yeung, T. Hahn, B. Dromey, S. Herzer, S. Fuchs, A. G. Pour, E. Eckner, M. Behmke, M. Cerchez, O. J??ckel, D. Hemmers, T. Toncian, M. C. Kaluza, A. Belyanin, G. Pretzler, O. Willi, A. Pukhov, M. Zepf, and G. G. Paulus, "Harmonic generation from relativistic plasma surfaces in ultrasteep plasma density gradients," Phys. Rev. Lett., vol. 109, no. 12, p. 125002, Sep. 2012.

[51]  M. Roth, D. Jung, K. Falk, N. Guler, O. Deppert, M. Devlin, A. Favalli, J. Fernandez, D. Gautier, M. Geissel, R. Haight, C. E. Hamilton, B. M. Hegelich, R. P. Johnson, F. Merrill, G. Schaumann, K. Schoenberg, M. Schollmeier, T. Shimada, T. Taddeucci, J. L. Tybo, F. Wagner, S. A. Wender, C. H. Wilde, and G. A. Wurden, "Bright laser-driven neutron source based on the relativistic transparency of solids," Phys. Rev. Lett., vol. 110, no. 4, p. 44802, Jan. 2013.

[52]  H. N. Chapman, A. Barty, M. J. Bogan, S. Boutet, M. Frank, S. P. Hau-Riege, S. Marchesini, B. W. Woods, S. Bajt, W. H. Benner, R. A. London, E. Plönjes, M. Kuhlmann, R. Treusch, S. Düsterer, T. Tschentscher, J. R. Schneider, E. Spiller, T. Möller, C. Bostedt, M. Hoener, D. A. Shapiro, K. O. Hodgson, D. van der Spoel, F.

Burmeister, M. Bergh, C. Caleman, G. Huldt, M. M. Seibert, F. R. N. C. Maia, R. W. Lee, A. Szöke, N. Timneanu, and J. Hajdu, "Femtosecond diffractive imaging with a soft-X-ray free-electron laser," Nat. Phys., vol. 2, no. 12, pp. 839–843, Dec. 2006.

[53]  H. N. Chapman and K. A. Nugent, "Coherent lensless X-ray imaging," Nat. Photonics, vol. 4, no. 12, pp. 833–839, Dec. 2010.

[54]  A. Barty, J. Küpper, and H. N. Chapman, "Molecular Imaging Using X-Ray Free-Electron Lasers," Annu. Rev. Phys. Chem., vol. 64, no. 1, pp. 415–435, Apr. 2013.

[55]  R. Neutze, R. Wouts, D. van der Spoel, E. Weckert, and J. Hajdu, "Potential for biomolecular imaging with femtosecond X-ray pulses.," Nature, vol. 406, no. 6797, pp. 752–757, Aug. 2000.

[56]  T. Kluge, C. Gutt, L. G. Huang, J. Metzkes, U. Schramm, M. Bussmann, and T. E. Cowan, "Using X-ray free-electron lasers for probing of complex interaction dynamics of ultra-intense lasers with solid matter," Phys. Plasmas, vol. 21, no. 3, p. 33110, Mar. 2014.

[57]  T. Kluge, M. Bussmann, H.-K. Chung, C. Gutt, L. G. Huang, M. Zacharias, U. Schramm, and T. E. Cowan, "Nanoscale femtosecond imaging of transient hot solid density plasmas with elemental and charge state sensitivity using resonant coherent diffraction," Phys. Plasmas, vol. 23, no. 3, p. 33103, Mar. 2016.

[58]  F. Brunel, "Anomalous absorption of high intensity subpicosecond laser pulses," Phys. Fluids, vol. 31, no. 9, pp. 2714–2719, 1988.

[59]  F. N. Beg, A. R. Bell, A. E. Dangor, C. N. Danson, A. P. Fews, M. E. Glinsky, B. A. Hammel, P. Lee, P. A. Norreys, and M. Tatarakis, "A study of picosecond laser–solid interactions up to 10 $^{19}$ W cm $^{-2}$," Phys. Plasmas, vol. 4, no. 2, pp. 447–457, Feb. 1997.

[60]  P. Mulser, D. Bauer, and H. Ruhl, "Collisionless laser-energy conversion by anharmonic resonance," Phys. Rev. Lett., vol. 101, no. 22, p. 225002, Nov. 2008.

[61]  C. Gahn, G. D. Tsakiris, A. Pukhov, J. Meyer-ter-Vehn, G. Pretzler, P. Thirolf, D. Habs, and K. J. Witte, "Multi-MeV Electron Beam Generation by Direct Laser Acceleration in High-Density Plasma Channels," Phys. Rev. Lett., vol. 83, no. 23, pp. 4772–4775, 1999.

[62]  A. Macchi, F. Cornolti, and F. Pegoraro, "Two-surface wave decay," Phys. Plasmas, vol. 9,

no. 5, p. 1704, May 2002.

[63] M. Schollmeier, A. B. Sefkow, M. Geissel, A. V. Arefiev, K. A. Flippo, S. A. Gaillard, R. P. Johnson, M. W. Kimmel, D. T. Offermann, P. K. Rambo, J. Schwarz, and T. Shimada, "Laser-to-hot-electron conversion limitations in relativistic laser matter interactions due to multi-picosecond dynamics," Phys. Plasmas, vol. 22, no. 4, p. 43116, Apr. 2015.

[64] M. Sherlock, E. G. Hill, R. G. Evans, S. J. Rose, and W. Rozmus, "In-depth plasma-wave heating of dense plasma irradiated by short laser pulses," Phys. Rev. Lett., vol. 113, no. 25, p. 255001, 2014.

[65] Y. Sentoku, E. D'Humières, L. Romagnani, P. Audebert, and J. Fuchs, "Dynamic control over mega-ampere electron currents in metals using ionization-driven resistive magnetic fields," Phys. Rev. Lett., vol. 107, no. 13, p. 135005, Sep. 2011.

[66] S. D. Gilev and A. M. Trubachev, "Metallization of silicon in a shock wave: the metallization threshold and ultrahigh defect densities," J. Phys. Condens. Matter, vol. 16, no. 46, pp. 8139–8153, 2004.

[67] P. M. Celliers, A. Ng, G. Xu, and A. Forsman, "Thermal Equilibrium in a Shock Wave," Phys. Rev. Lett., vol. 68, no. 15, p. 2305, 1992.

[68] T. G. White, J. Vorberger, C. R. D. Brown, B. J. B. Crowley, P. Davis, S. H. Glenzer, J. W. O. Harris, D. C. Hochhaus, S. Le Pape, T. Ma, C. D. Murphy, P. Neumayer, L. K. Pattison, S. Richardson, D. O. Gericke, and G. Gregori, "Observation of inhibited electron-ion coupling in strongly heated graphite," Sci. Rep., vol. 2, p. 889, 2012.

[69] O. Glatter and O. Kratky, Small angle x-ray scattering. London: Academic Press Inc. Ltd., 1982.

[70] W. C. Michels, A. L. Patterson, and R. K. Wangsness, Elements of Modern Physics, 2nd ed., vol. 20, no. 1. Sussex (UK): John Wiley & Sons, Ltd., 1952.

[71] H. K. Chung, M. H. Chen, and R. W. Lee, "Extension of atomic configuration sets of the Non-LTE model in the application to the K?? diagnostics of hot dense matter," High Energy Density Phys., vol. 3, no. 1–2, pp. 57–64, 2007.

[72] Neutron, X-rays and Light. Scattering Methods Applied to Soft Condensed Matter - 1st Edition ISBN: 9781493302260 - 9780080930138. .

[73] R. F. Smith, C. A. Bolme, D. J. Erskine, P. M. Celliers, S. Ali, J. H. Eggert, S. L. Brygoo, B. D. Hammel, J. Wang, and G. W. Collins, "Heterogeneous flow and brittle failure in shock-compressed silicon," J. Appl. Phys., vol. 114, no. 13, p. 133504, 2013.

[74] W. C. Michels, A. L. Patterson, and R. K. Wangsness, Elements of Modern Physics, vol. 20, no. 1. 1952.

[75] S. K. Sinha, E. B. Sirota, S. Garoff, and H. B. Stanley, "X-ray and neutron scattering from rough surfaces," Phys. Rev. B, vol. 38, no. 4, pp. 2297–2311, 1988.